



**CHALMERS**  
UNIVERSITY OF TECHNOLOGY

## **Decomposition pathways in nano-lamellar CVD $\text{Ti}_{0.2}\text{Al}_{0.8}\text{N}$**

Downloaded from: <https://research.chalmers.se>, 2024-03-20 12:05 UTC

Citation for the original published paper (version of record):

Bäcke, O., Kalbfleisch, S., Stiens, D. et al (2023). Decomposition pathways in nano-lamellar CVD  $\text{Ti}_{0.2}\text{Al}_{0.8}\text{N}$ . Materialia, 30. <http://dx.doi.org/10.1016/j.mtla.2023.101833>

N.B. When citing this work, cite the original published paper.



## Full length article

Decomposition pathways in nano-lamellar CVD  $\text{Ti}_{0.2}\text{Al}_{0.8}\text{N}$ 

Olof Bäcké<sup>a</sup>, Sebastian Kalbfleisch<sup>b</sup>, Dirk Stiens<sup>c</sup>, Thorsten Manns<sup>c</sup>, Anton Davydok<sup>d</sup>,  
Mats Halvarsson<sup>a</sup>, Magnus Hörnqvist Colliander<sup>a,\*</sup>

<sup>a</sup> Department of Physics, Chalmers University of Technology, Gothenburg, Sweden

<sup>b</sup> MAX IV Laboratory, Lund, Sweden

<sup>c</sup> Walter AG, Tübingen, Germany

<sup>d</sup> Helmholtz-Zentrum Hereon, Institute of Materials Physics, Geesthacht, Germany

## ARTICLE INFO

## Keywords:

Chemical vapour deposition (CVD)

(Ti,Al)N

Phase stability

Phase separation

Coatings

## ABSTRACT

Recent progress in chemical vapour deposition (CVD) technology has enabled synthesis of metastable cubic  $\text{Ti}_{1-x}\text{Al}_x\text{N}$  coatings with  $x$  as high as 0.8–0.9. These coatings have unique micro- and nano-structures consisting of grains with epitaxially grown nanolamellae with different Al/Ti ratios, and exhibit exceptional hardness and resistance to wear and oxidation. Here, the thermal stability and decomposition of nano-lamellar CVD  $\text{Ti}_{0.2}\text{Al}_{0.8}\text{N}$  at temperatures between 800 and 1000 °C have been investigated using a combination of cross-sectional transmission X-ray nano-diffraction and scanning transmission electron microscopy. The decomposition started by formation of hexagonal AlN (h-AlN) in the grain boundaries throughout the coating. Below 900 °C, only limited further decomposition of the grain interiors occurred. At higher temperatures the formation of grain boundary h-AlN was followed by a bulk transformation of the nano-lamellar structure, starting at the top of the coating and subsequently sweeping inwards. The bulk transformation occurred initially through spinodal decomposition, followed by transformation of the Al-rich cubic phase to h-AlN, leading to a coarsened structure with Ti-rich domains in a h-AlN matrix. The behaviour is explained by the higher capability of grain boundaries and free surfaces to accommodate the volumetric expansion from the h-AlN formation. The results increase our understanding of the complicated decomposition processes in these metastable cubic coatings, which are of utmost importance from both technological and scientific perspectives.

## 1. Introduction

(Ti,Al)N with different Ti:Al ratios (more precisely written  $\text{Ti}_{1-x}\text{Al}_x\text{N}$ ) and a face centred cubic (fcc) structure deposited by physical vapour deposition (PVD) has emerged as an extremely successful material system for wear resistant coatings in tooling applications [1–3]. The critical properties of the fcc (Ti,Al)N phase, such as hardness, wear resistance and oxidation resistance, all increase with increasing Al content, up to the point where hexagonal AlN (hereafter called h-AlN) begins to form [4–7]. For PVD this occurs around  $x = 0.6$ – $0.7$  [7–12], and the need for further property improvement by increasing the Al content has spurred the development of alternative synthesis routes. In spite of the higher deposition temperatures in chemical vapour deposition (CVD) processes, which would be expected to promote the stable two-phase fcc+hcp microstructure during deposition, recently developed low-pressure CVD processes have been shown capable of producing single phase fcc (Ti,Al)N coatings with  $x$  exceeding 0.9 [13–21], yielding exceptional properties [13,14,16–18,20].

A unique feature of CVD (Ti,Al)N coatings is their complex microstructure where the relatively large ( $\mu\text{m}$  range) elongated grains consist of epitaxial nanosized lamellae corresponding to periodic variations in the Ti:Al ratio, effectively giving each grain a multilayered structure [17,19,21–23]. Typical average compositions of “Ti-rich” Ti(Al)N and “Al-rich” Al(Ti)N nano-lamellae obtained using scanning transmission electron microscopy energy dispersive X-ray spectroscopy (STEM-EDX) are  $\text{Ti}_{0.5}\text{Al}_{0.5}\text{N}$  and  $\text{Ti}_{0.1}\text{Al}_{0.9}\text{N}$ , respectively. Furthermore, a recent investigation using atom probe tomography (APT) have shown large compositional variations *within* the lamellae [24]. In particular, compositions ranging from  $\text{Ti}_{0.7}\text{Al}_{0.3}\text{N}$  to  $\text{Ti}_{0.1}\text{Al}_{0.9}\text{N}$  could be found within single Ti(Al)N lamellae, which should therefore not be seen as homogeneous structures but a network of domains with elevated Ti content embedded in what is effectively a continuous Al(Ti)N matrix. Al(Ti)N lamellae are usually reported to be thicker than Ti(Al)N and the periodicity can vary, but is usually found to be around a few to some tens of nm [21].

\* Corresponding author.

E-mail address: [magnus.colliander@chalmers.se](mailto:magnus.colliander@chalmers.se) (M. Hörnqvist Colliander).

<https://doi.org/10.1016/j.mtla.2023.101833>

Received 11 November 2022; Accepted 20 June 2023

Available online 30 June 2023

2589-1529/© 2023 The Author(s). Published by Elsevier B.V. on behalf of Acta Materialia Inc. This is an open access article under the CC BY license (<http://creativecommons.org/licenses/by/4.0/>).

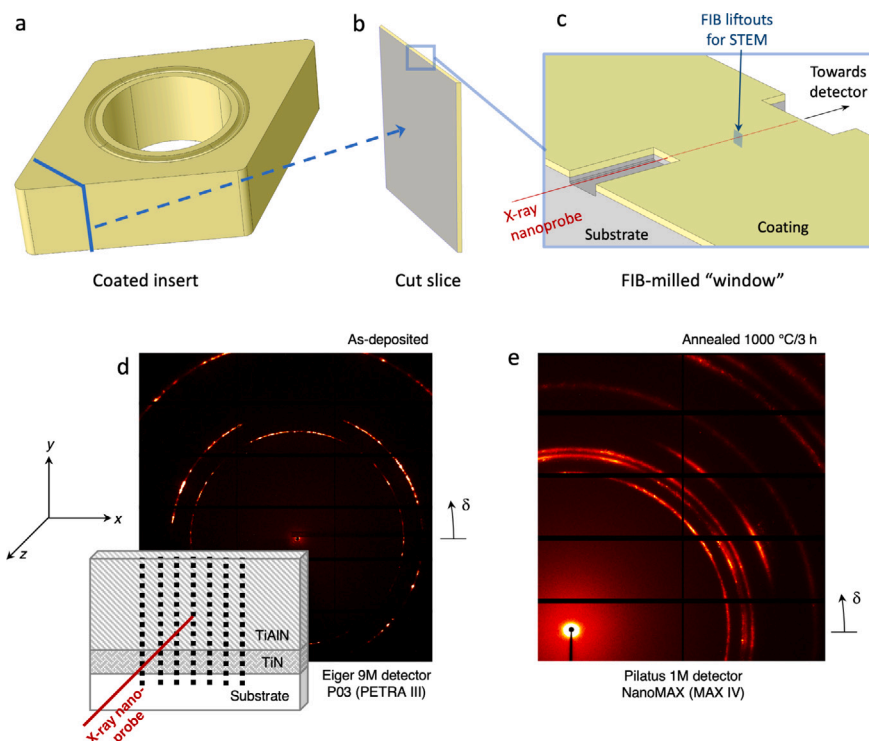


Fig. 1. Schematic of the specimen preparation and nano-diffraction set-up. (a) Coated insert, where the blue lines indicate where the 300  $\mu\text{m}$  thick slice (b) is cut. (c) FIB milled window on the top of the slice for CSTnD investigations. FIB milling was also used to extract TEM thin-foils from the investigated part of coatings for post-CSTnD STEM investigations. (d) CSTnD set-up, including a typical detector image from the as-deposited coating obtained at P03 (PETRA III). (For interpretation of the references to colour in this figure legend, the reader is referred to the web version of this article.)

A fundamental aspect of coating performance is thermal stability, and the fcc (Ti,Al)N phase is metastable and will decompose into TiN+h-AlN at elevated temperatures. The decomposition pathways are expected to be complex as a result of the periodic chemical variations in the nano-lamellar structure, and the microstructure evolution during annealing has therefore received increasing attention. Age hardening (spinodal decomposition) and subsequent overaging (h-AlN formation) have been shown to occur in nano-lamellar CVD coatings [13,17,18,20,22,23,25,26]. The temperature range and kinetics of spinodal decomposition varies between the studies, likely due to differences in chemistry, deposition conditions, micro- and nanostructures and experimental approaches. Furthermore, as shown for AlCrN and AlCr(S)N coatings, the residual stress state plays a critical role for the onset of spinodal decomposition [27,28].

Recently, investigations of coatings pre-annealed in vacuum for 5 min at different temperatures showed that the decomposition is inhomogeneous through the coating thickness [25,26]. The process had progressed much further in the upper part of the coating, leaving a visible boundary between the outer transformed zone and the inner untransformed material. TEM observations across the transition zone between transformed and untransformed material in a coating pre-annealed at 1050  $^{\circ}\text{C}$  clearly showed the occurrence of spinodal decomposition (splitting of the (Ti,Al)N reflections in selected area diffraction patterns) and formation of h-AlN [25]. Inhomogeneous initiation of the decomposition due to e.g. heterogeneous chemistry or strain was proposed as a reason for the higher stability of the inner part of the coating, as the smaller grain size and lower defect density could delay the process. Furthermore, the microstructure of a fully decomposed coating (annealed for 5 min at 1300  $^{\circ}\text{C}$ ) showed globular TiN particles in a h-AlN matrix. In the fully decomposed coating the authors noted particles at the grain boundaries, which were identified as TiN based on contrast in dark field STEM. In this state, APT measurements yielded chemical compositions very close to pure TiN and AlN for the two phases. In addition, regions of untransformed

fcc (Ti,Al)N were observed within the transformed part of the coating annealed at 1050  $^{\circ}\text{C}$  for 5 min [26].

In spite of the details revealed by the studies above, and in particular that by Tkadletz et al. [25], it is clear that the decomposition process is still not fully understood. Motivated by the observed through-thickness gradients in the decomposition [25,26], and the still very limited detailed studies of the microstructure during decomposition we combine scanning transmission electron microscopy (STEM) and cross-sectional transmission X-ray nano-diffraction (CSTnD) [29] to investigate the decomposition of nano-lamellar CVD  $\text{Ti}_{0.2}\text{Al}_{0.8}\text{N}$ . While TEM and STEM offers unrivalled spatial resolution for determining local structure and chemistry, the drawback is the limited statistics obtained from electron transparent samples. CSTnD, which employs hard X-ray nano-probes available at dedicated synchrotron beamlines to collect diffraction patterns from carefully prepared samples with an area detector in transmission geometry, have been used to perform phase distribution, texture and residual stress/strain mapping in multiple different coating systems (including (Ti,Al)N based thin films, see e.g. [16,30,31]). By systematically studying samples subjected to long-term annealing (3 h) in Ar at temperatures in the range 800–1000  $^{\circ}\text{C}$  we are able to follow the transformation and propose a decomposition route involving initial formation of h-AlN at the grain boundaries, followed by a bulk transformation of grain interiors through spinodal decomposition which initiates at the outer surface and the transformation front subsequently sweeps inwards through the coating.

## 2. Experimental

### 2.1. Coating synthesis and thermal annealing

(Ti,Al)N/TiN bi-layer coatings with an approximate total thickness of 4.0–5.7  $\mu\text{m}$  were deposited on 94 wt% WC/6 wt% Co cemented carbide inserts with an SNMA120412 geometry in an industrial CVD

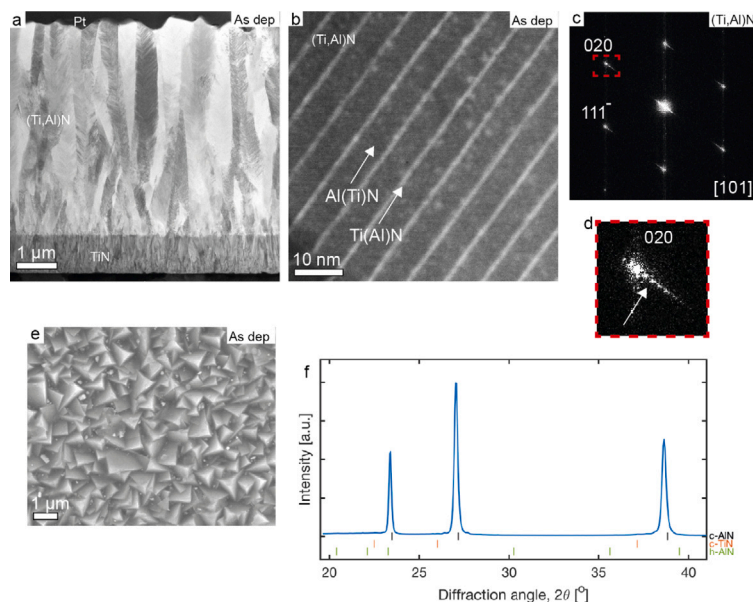


**Fig. 2.** (a) BF STEM micrograph of cross section of the (Ti,Al)N coating before thermal annealing. (b)–(c) HAADF STEM micrograph and accompanying FFT of the nano-lamellae structure in the as-deposited coating. (d) Close up of FFT in (c), showing satellite reflections stemming from the nano-lamellae structure. (e) Top view SEM micrograph of the coating before thermal annealing. (f) Diffractogram obtained after summing all frames from the as-deposited sample (except the region where the TiN and (Ti,Al)N layers overlapped) and integrating of over the full available azimuthal range. Ideal position of cubic AlN (c-AlN), TiN and h-AlN are indicated. No signs of h-AlN or TiN can be seen.

reactor. The inserts were polished and cleaned with ethanol prior to deposition. The TiN layer, with an approximate thickness of 1  $\mu\text{m}$ , was deposited onto the inserts at a temperature of 850  $^{\circ}\text{C}$  and a pressure below 150 mbar, using  $\text{TiCl}_4$ ,  $\text{N}_2$  and  $\text{H}_2$  as precursor and carrier gases. The (Ti,Al)N layer was deposited on top of the TiN layer at a temperature of 700  $^{\circ}\text{C}$  and at a pressure below 25 mbar, using  $\text{TiCl}_4$ ,  $\text{AlCl}_3$  and  $\text{NH}_3$  as precursor and carrier gases. The overall composition was measured by energy dispersive X-ray spectroscopy (EDS) to  $\text{Ti}_{0.2}\text{Al}_{0.8}\text{N}$  [21]. To investigate the thermal stability of the coatings, inserts were subjected to 3 h isothermal annealing treatments in Ar atmosphere at temperatures ranging from 800 to 1000  $^{\circ}\text{C}$ .

## 2.2. Cross-sectional transmission nano-diffraction

In order to map the microstructure in the coatings using CSTnD, slices with approximate thicknesses around 200–300  $\mu\text{m}$  were cut from the inserts by a low speed diamond saw, Fig. 1(a)–(b). Areas with dimensions (width  $\times$  depth) of around  $80 \times 12 \mu\text{m}^2$  were locally thinned down to 60–100  $\mu\text{m}$  thickness using focused ion beam milling in an FEI Versa 3D focused ion beam-scanning electron microscope (FIB-SEM), Fig. 1(c). CSTnD experiments were performed at the Nanofocus endstation [32] of the P03 beamline [33] at the PETRA III synchrotron, DESY, Hamburg, Germany (as-deposited coating and samples annealed at 800 and 850  $^{\circ}\text{C}$ ) and at the NanoMAX beamline [34,35] at the 3 GeV storage ring of the MAX IV synchrotron, Lund, Sweden (samples annealed at 900, 950 and 1000  $^{\circ}\text{C}$ ). At P03 an energy of 12.98 keV (X-ray wavelength  $\lambda=0.955 \text{ \AA}$ ) and beam size 350 nm was used, while experiments at NanoMAX was performed at 14.3 keV (X-ray wavelength  $\lambda=0.867 \text{ \AA}$ ) giving a spot size at the focus position of around 62 nm [36]. Area detectors were placed downstream of the sample position (Dectris Eiger 9M with a sample-to-detector distance of 196 mm at P03, and Dectris Pilatus 1M at 272 mm at NanoMAX). The detector was off-set at NanoMAX due to the larger sample-to-detector distance, in order to provide access to larger diffraction angles, and hence only quarter diffraction rings were captured on the detector. At P03 full rings could be collected. Calibration was performed using  $\text{LaB}_6$  (P03) and Si (NanoMAX) standards.

Fig. 1(d) shows a schematic of the setup, including a typical detector image from the as-deposited coating acquired at P03, and Fig. 1(e)

shows a detector image from the sample annealed at 1000  $^{\circ}\text{C}$  collected at NanoMAX. The sample was moved relative to the beam in a rectangular grid and diffraction patterns were collected at each position using exposure times of 5 s. The step size was 350 nm at P03, and 70–100 nm at NanoMAX (different for different samples) in the vertical direction ( $y$  in Fig. 1). The number of points in a scan varied between samples, but in all cases the entire coating and the top part of the substrate was measured. At P03 three vertical linescans (at constant  $x$ , see Fig. 1) were performed, while between 12 and 60 linescans were used for each sample at NanoMAX to increase the statistics with the smaller beam. Subsequently all frames at the same height in the coating ( $y$ ) were averaged to provide a single average diffraction pattern for each position. The averaged frames were reduced to 1D diffractograms using PyFAI v.0.20.0 [37], and single peaks were fitted using Pseudo-Voigt shape functions in MATLAB using the Line-Profile Analysis Software (LIPRAS) interface [38]. When analysing the data from NanoMAX the full available azimuthal range ( $-10^{\circ} \leq \delta \leq 100^{\circ}$ ) was integrated for phase determination, while only the range  $0^{\circ} \leq \delta \leq 180^{\circ}$  was used in the case of data obtained at P03, since the bottom half of the ring was partially shadowed by the sample.

## 2.3. Electron microscopy

Cross sectional thin-foil specimens were extracted from the regions investigated by CSTnD after completed diffraction experiments with a FEI Versa 3D FIB-SEM. The same system was used to collect SEM top view images of the (Ti,Al)N coatings. STEM characterization of the thin-foil specimen was performed using an FEI Titan 80–300 TEM/STEM instrument operated at 300 kV equipped with a high angle annular dark-field (HAADF) detector, a bright field (BF) detector and an Oxford X-ray EDS detector.

## 3. Results and discussion

### 3.1. As-deposited microstructure

In the as-deposited state, the (Ti,Al)N coatings consist of elongated grains with typical lateral widths of a few hundred nm and a height (in the growth direction) of a few  $\mu\text{m}$ , see Fig. 2(a). While the macroscopic



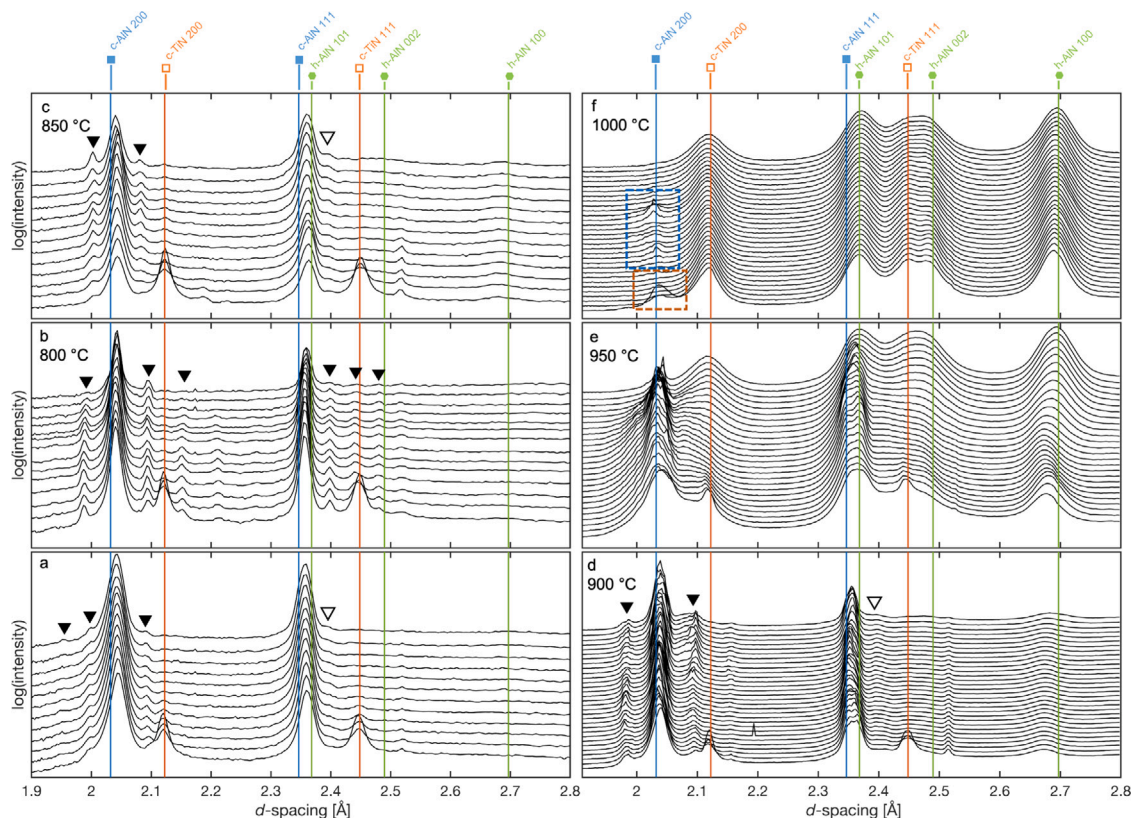


**Fig. 3.** Diffractograms (logarithm of intensity vs.  $d$ -spacing) as a function of position in the coating. The bottom curve in each panel corresponds to the (Ti,Al)N/TiN interface and the top curve corresponds to the top of the coating. (a) As-deposited coating; (b) annealed at 800 °C; (c) annealed at 850 °C; (d) annealed at 900 °C; (e) annealed at 950 °C; (f) annealed at 1000 °C. Filled arrowheads (▼) denote superlattice satellite peaks, open arrowheads (▽) indicate diffraction from Ti(Al)N lamellae. The dashed red and blue squares in (f) indicates the presence of remaining fcc (Ti,Al)N at the (Ti,Al)N interface and within the transformed region, respectively. The small peaks occasionally seen just above 2.2 and 2.5 Å originate from the substrate due to small misalignment of the X-ray beam and the sample and possible uneven FIB milling leading to intersection of the primary beam with substrate material up- or downstream of the FIB milled window. (For interpretation of the references to colour in this figure legend, the reader is referred to the web version of this article.)

growth direction of the grains is  $\langle 111 \rangle$ , the grains actually grow by successive addition of  $\{100\}$  layers during deposition [21], which creates pyramidal profiles consisting of the three  $\{100\}$  facets at the free top surface, see Fig. 2(e). The previously described nano-lamellae structure, with alternating Ti(Al)N and Al(Ti)N lamellae, can be seen in Fig. 2(b) where the broader lamellae are enriched in Al and the comparatively thinner lamellae are enriched in Ti. As the lamellae are created during deposition on the  $\{100\}$  facets, they are all perpendicular to a  $\langle 100 \rangle$  direction (see the FFT in Fig. 2(c) extracted from Fig. 2(b)). Fig. 2(d) shows a magnified view of the 020 FFT in Fig. 2(b), where superlattice reflections from the nano-lamellar structure are clearly visible.

Fig. 2(f) shows a CSTnD diffractogram obtained after summing all frames from the as-deposited sample (except the region where the TiN and (Ti,Al)N layers overlapped) and integrating of over the full available azimuthal range. The observed (Ti,Al)N peaks are approximately symmetric, and their position are close to pure cubic AlN (c-AlN). The lattice parameter obtained by Pawley refinement using GSAS-II [39] indicates a value of 4.078(2) Å, corresponding to a chemical composition of approximately  $\text{Ti}_{0.1}\text{Al}_{0.9}\text{N}$  [40], as expected since the main contribution to the diffractogram comes from the Al(Ti)N lamellae. Obvious signs of smaller broad peaks associated with the Ti(Al)N nano-lamellae, as reported by e.g. Saringer et al. [20] and Tkadletz et al. [26], are not clearly visible here due to the linear intensity scale, but are present and will be discussed later. No signs of h-AlN can be seen.

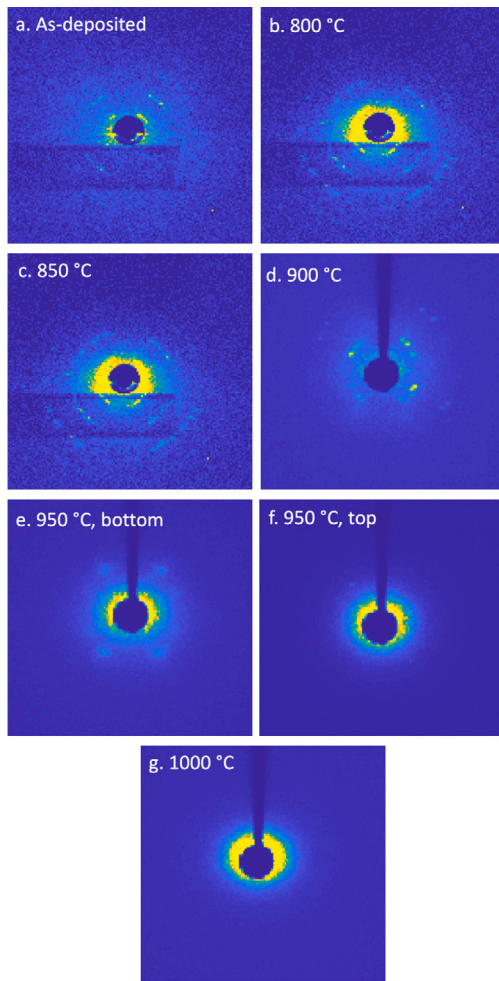
### 3.2. Microstructure of annealed coatings

Fig. 3 shows the integrated 1D diffractograms for the different annealing conditions. The bottom curve in each panel corresponds to

the (Ti,Al)N/TiN interface (where TiN 111 and 200 peaks from the top of the TiN layer can be seen) and the top curve corresponds to the top of the coating. From Fig. 3(a) the coating appears to be single phase (Ti,Al)N with no signs of h-AlN. With the logarithmic intensity scale a small shoulder can be seen at the high- $d$  side of the 111 peaks in Fig. 3(a),(c) and (d), at  $d$ -spacings of around 2.4 Å (marked by open arrowheads). This resembles the observed Ti(Al)N peaks from powdered (Ti,Al)N CVD coatings studied by high energy synchrotron diffraction [20], and presumably originate from the Ti(Al)N lamellae, as the position corresponds to a lattice parameter of around 4.16 Å, equivalent to a composition of  $\text{Ti}_{0.5}\text{Al}_{0.5}\text{N}$ . Shoulders are not discernible at the 111 peak in Fig. 3(b), neither at any of the 200 peaks in Fig. 3(a)–(d) due to overlap with superlattice satellite peaks. These satellite peaks (marked by black arrowheads) are most clearly visible around the 200 peak but, in particular in the sample annealed at 800 °C, also around the 111 peak. The superlattice periodicity can be determined from the relationship

$$\Lambda = \frac{\lambda}{2|\sin \theta_i - \sin \theta_{i\pm 1}|} = \frac{d_i d_{i\pm 1}}{|d_i - d_{i\pm 1}|} \quad (1)$$

where  $\theta_i$  and  $\theta_{i\pm 1}$  are the half diffraction angles for two consecutive satellites, and  $d_i$  and  $d_{i\pm 1}$  are the corresponding  $d$ -spacing. The resulting average superlattice periodicities in the present case are determined to approximately 9.1 nm (as-deposited), 7.9 nm (800 °C), 10.2 nm (850 °C) and 7.5 nm (900 °C). After annealing at 950 °C superlattice peaks can no longer be clearly observed, but careful examination of the shoulders around the 200 peaks show traces corresponding to a periodicity of 10.5–11 nm, which disappear in the top-most part of the coating. After annealing at 1000 °C the superlattice peaks are absent.



**Fig. 4.** Detector images corresponding to the small angle scattering (SAS) region for (a) as-deposited coating; (b)–(d) coatings annealed at 800–900 °C; (e) and (f) bottom and top part of the coating annealed at 950 °C; (g) Coating annealed at 1000 °C. Note the symmetry in the SAS pattern due to the texture of the coatings and epitaxial growth of nano-lamellae.

This is consistent with observations of the small angle scattering (SAS) region close to the beam stop, Fig. 4. Multiple order SAS maxima from the superlattice periodicity can be seen in the as-deposited coating and after annealing at temperatures up to 900 °C (Fig. 4(a)–(d)). The periodicities derived from the position of the  $n^{\text{th}}$  order maxima  $Q_m$

$$\Lambda_{\text{SAS}} = \frac{2\pi n}{Q_m} \quad (2)$$

were found to match those measured from the satellite peak spacing ( $\Lambda_{\text{SAS}}$  = 8.8, 7.9, 10.8 and 7.4 nm for as-deposited, 800, 850 and 900 °C, respectively). After annealing at 950 °C, the SAS maxima is present (although much weaker) in the lower part of the coating (e), but disappear in the transformed part closer to the top (f). Annealing at 1000 °C completely removes the superlattice SAS signal throughout the coating thickness (g). The superlattice periodicity derived from the CSTnD measurements agree closely with values extracted from the STEM FFTs.

In Fig. 3(c) we clearly see the presence of a weak and broad h-AlN 100 peak after 850 °C annealing, which is not present in the as-deposited microstructure or after annealing at 800 °C (Fig. 3(a) and (b)). The observed h-AlN 100  $d$ -spacing is approximately 2.68 Å close to the interface, slightly smaller than stoichiometric h-AlN (2.70 Å). This is unlikely to be a chemical effect, as the lattice parameter should increase if Ti is incorporated. The small lattice parameter is presumably

a result of the surrounding material restricting the volume expansion (around 20 %) from the cubic-to-hexagonal transformation, resulting in compressive strains in the hexagonal phase. Towards the top of the coating the lattice parameter is close to the expected value, consistent with the proximity to the free top surface, which allows relaxation of the stresses by out-of-plane deformation. The h-AlN peaks are more pronounced, although still very weak and broad, after annealing at 900 °C (Fig. 3(d)).

The through-thickness variation in decomposition after annealing at 950 °C can be clearly seen from the changes in diffractograms with position (Fig. 3(e)). The  $d$ -spacing of the h-AlN 100 peak shows large variations across the height, and approaches the value expected for the stoichiometric phase only towards the top. The same is seen for the TiN 200 peak, which more resembles a shoulder on the high- $d$  side of the (Ti,Al)N 200 peak close to the interface, but clearly forms a separate peak with close-to-ideal  $d$ -spacing towards the top. The intensities of h-AlN 100 and TiN 200 also increases significantly towards the top. There is a splitting of the (Ti,Al)N 111 peak which persists almost throughout the coating thickness. At the very top however, a single peak belonging to h-AlN 101 is found instead, indicating that the decomposition has progressed much further there. On the high- $d$  side of the peak, a broad shoulder corresponding to TiN 111, overlapping with a second shoulder belonging to h-AlN 002, can be seen. The broad, almost flat, appearance of the TiN peak suggest that there is a wide range of  $d$ -spacings present simultaneously, representing a variation in composition, which is consistent with chemical modulations associated with spinodal decomposition. Towards the top of the coating, only a single broad composite TiN/h-AlN peak remains.

The almost fully decomposed structure after the 1000 °C anneal is shown in Fig. 3(f). A narrow region at the original (Ti,Al)N/TiN interface (red dashed square) is all that remains of the original (Ti,Al)N phase. Clear peaks corresponding to TiN and h-AlN peaks are present throughout the coating, with  $d$ -spacings only slightly smaller than ideal, indicating that the residual stress is close to zero. The blue dashed square indicates the presence of an isolated “pocket” of remaining (Ti,Al)N present at mid-thickness.

### 3.3. Decomposition route

While the CSTnD data clearly shows the gradual appearance of h-AlN and TiN as a function of thickness in the coating, it does not reveal *where* in the microstructure these phases form. To obtain further details on the decomposition process HAADF STEM imaging was used, for which the dominating contrast mechanism is  $Z$ -contrast. The density of h-AlN is lower than the density of (Ti,Al)N, and domains of h-AlN will thus be darker compared to domains of (Ti,Al)N in HAADF STEM micrographs. Similarly, any domains of pure TiN will be brighter than (Ti,Al)N domains. However, contrast variations in HAADF STEM micrographs are not by themselves enough to determine if a domain is (Ti,Al)N, TiN or h-AlN. The results obtained through HAADF STEM imaging were thus compared with the CSTnD measurements and further verified by extracting FFTs from either high resolution HAADF or BF STEM micrographs. It was found that the formation of h-AlN and TiN during annealing can be divided into two different cases: (i) bulk decomposition of the grain interiors starting at the coating surface; and (ii) formation of h-AlN and TiN along the grain boundaries. These cases are discussed separately below.

#### 3.3.1. Transformation in the grain interior

The bulk decomposition of (Ti,Al)N into h-AlN and TiN starts at the surface and spreads down through the coating, see Figs. 5(a)–(d). The onset at the coating surface is visible after annealing at 900 °C, where it was found that some grains at the coating surface had begun to transform, see Figs. 5(b) and (e). The grains are only partly transformed, with the transformed volume stretching some 200–300 nm into the coating. After annealing at 950 °C, the upper third of the coating



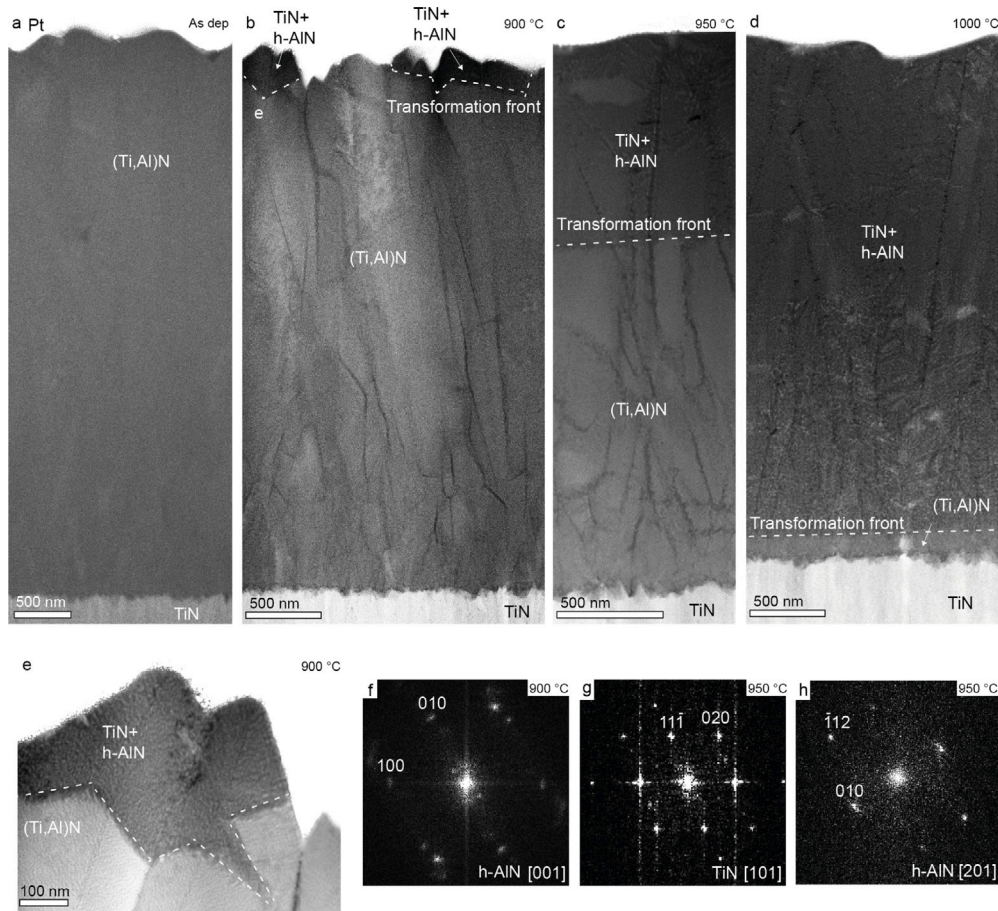


**Fig. 5.** HAADF STEM micrographs showing the overall microstructure of (a) the as-deposited coating; and coatings annealed at (b) 900 °C (b); (c) 950 °C; and (d) 1000 °C. (e) shows a small transformed zone at the top of the coating after annealing at 900 °C (see indication in (b) for position). (f)–(h) FFTs extracted from the transformed regions in the coatings annealed at 900 °C (f) and 950 °C (g, h), showing the formation of h-AlN and TiN. (f) is from a partly transformed grain similar to the one seen in (e), while (g) and (h) are extracted from a grain along the transformation front in the coating annealed at 950 °C.

have transformed, matching the CSTnD data, and the transformation front stretches roughly horizontally through the coating, see Fig. 5(c). Consistent with observations by Tkadletz et al. [25], the front does not follow grain boundaries, but regularly cuts through grains leaving partly transformed grains along the front. After annealing at 1000 °C, the whole coating has transformed from (Ti,Al)N to TiN and h-AlN, with the exception of small remnants of (Ti,Al)N grains spread through the decomposed coating, consistent with what have been reported by Tkadletz et al. [26], and a small strip of (Ti,Al)N above the lower (Ti,Al)N/TiN interface, see Fig. 5(d). High resolution STEM (HR STEM) was used to verify that the darker regions visible in the HAADF STEM micrographs above the transformations front are TiN and h-AlN. Grains bisected by the transformations front were tilted to a major zone axis and FFTs were extracted from the transformed part of the grains. Examples of this for the coatings annealed at 900 and 950 °C can be seen in Figs. 5(f)–(h). In both cases the FFTs show the decomposition of (Ti,Al)N and the formation of h-AlN.

Domains of untransformed (Ti,Al)N were found in the transformed regions of the coatings both after annealing at 950 and 1000 °C, see Figs. 6(a)–(c) and 7(a)–(c). This explains the observations of retained cubic phase within the coating seen in the CSTnD data (Fig. 3(f)). The untransformed domains are parts of prior (Ti,Al)N grains, rather than entire prior grains. The untransformed domains still keep the nano-lamellae structure, see Fig. 6(b), but the (Ti,Al)N lamellae are substantially broader (around 3 nm) compared to the as-deposited (Ti,Al)N lamellae (1.8 nm). The evolution of the nano-lamellae structure after annealing at different temperatures is discussed more in detail in Section 3.4.

The band of untransformed (Ti,Al)N found above the (Ti,Al)N/TiN interface after annealing at 1000 °C, see Fig. 6(a), is consistent with the CSTnD data in Fig. 3(f). The untransformed domains in the band do not correspond to small isolated grains, but are the lower parts of the larger columnar (Ti,Al)N grains where the nano-lamellae structure has been retained, see Fig. 6(c).

### 3.3.2. Transformation in the grain boundary regions

The second transformation case is the formation of small volumes of h-AlN and TiN along grain boundaries, which happens already after annealing at 800 °C (although the presence of h-AlN could not be detected by CSTnD, see Fig. 3(b), presumably due to the low volume fraction), and explains why the signal for h-AlN can be found throughout the whole coatings in the CSTnD data. Examples of grain boundary h-AlN formation after annealing at 800 and 850 °C can be seen in Fig. 8(a) and (b). After annealing at 900 °C, the amount of h-AlN visible at grain boundaries is larger compared to the coatings annealed at lower temperatures, see Fig. 8(c), matching the increase in signal for h-AlN that can be seen the CSTnD plot for 900 °C. Similarly, after annealing at 950 °C even larger volumes of h-AlN can be seen along the grain boundaries, see Fig. 8(d). After annealing at 950 °C, not only darker h-AlN domains but also smaller brighter domains are visible along grain boundaries. These are TiN domains visible due to the larger amount of (Ti,Al)N transforming along grain boundaries at this temperature. In the coatings annealed at 950 and 1000 °C, the transformed grain boundary volumes are still visible in regions that have fully transformed from (Ti,Al)N and can be seen to stretch through the transformed region of the coating, see Figs. 5(c,d) and 8(d,e). The formation of h-AlN and

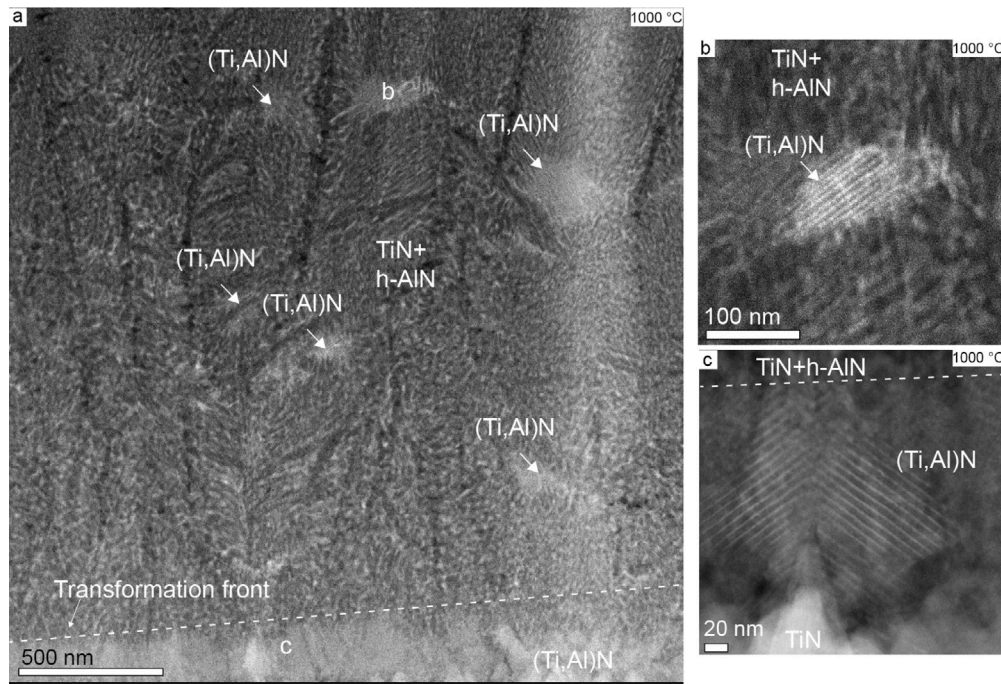


**Fig. 6.** HAADF STEM micrographs of coating after annealing at 1000 °C. (a) Overview of the coating where several untransformed (Ti,Al)N regions are marked. (b) and (c) show examples of remnants of (Ti,Al)N grains within the transformed part and along the lower (Ti,Al)N/TiN interface (locations indicated in (a)).

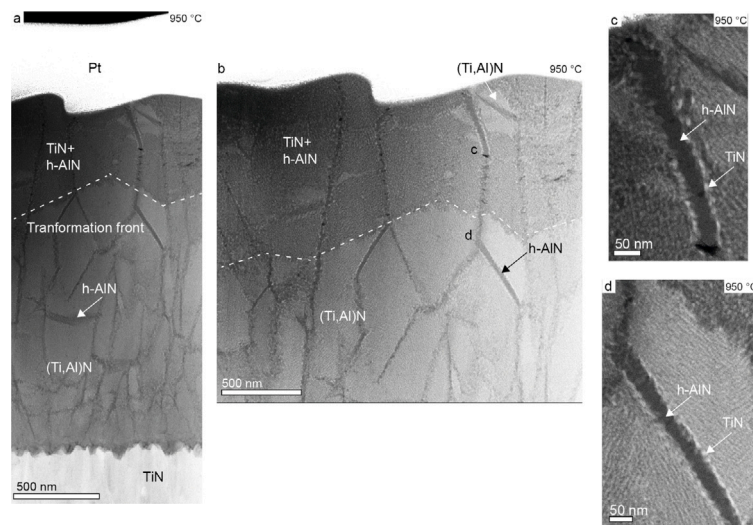


**Fig. 7.** HAADF STEM micrographs of the coating that has been annealed at 950 °C. Remnants of (Ti,Al)N grains and the grain boundaries are visible in the decomposed region.

TiN along grain boundaries was confirmed by HR-STEM. The domains have similar orientations as neighbouring (Ti,Al)N grains and thus by orienting a (Ti,Al)N grain along a major zone axis, FFTs could be extracted from the smaller domains that had formed along the grain boundaries of the grain in question. An example of this from the coating annealed at 950 °C can be seen in Fig. 9 and is discussed in further detail later.

The width of the transformed region at the grain boundaries after annealing at 1000 °C are similar from top to bottom in the coating, and after annealing at 950 °C the width of h-AIN domains along former grain boundaries does not change significantly between the transformed and non-transformed parts of the coating. This would indicate that the phase transformation happens first rapidly in volumes close to the grain boundaries until the transformed volumes reaches a critical size, after which the phase transformation slows down substantially,

allowing the transformed volumes along the grain boundaries to be enveloped by the bulk transformation front sweeping through the coating from the surface. This is further supported by the observation that while the width of the h-AIN domains forming along the grain boundaries increase noticeably after annealing at 900 °C compared to 850 °C, the increase in width slows down for higher temperatures. There is only a small increase in width after annealing at 950 °C compared to 900 °C, and no clear increase in width can be seen after annealing at 1000 °C compared to 950 °C. This is in contrast to the substantial difference in transformation of the bulk of the coatings, where nearly the whole coating is transformed after annealing at 1000 °C compared to only some pockets of transformed volume after annealing at 900 °C.

Interestingly, Figs. 5 and 6 reveal a significantly lower amount of grain boundary h-AIN in the innermost few hundred nm of the coatings. This was seen in all samples, independent of annealing temperature. The region with lower grain boundary h-AIN content correlates to the



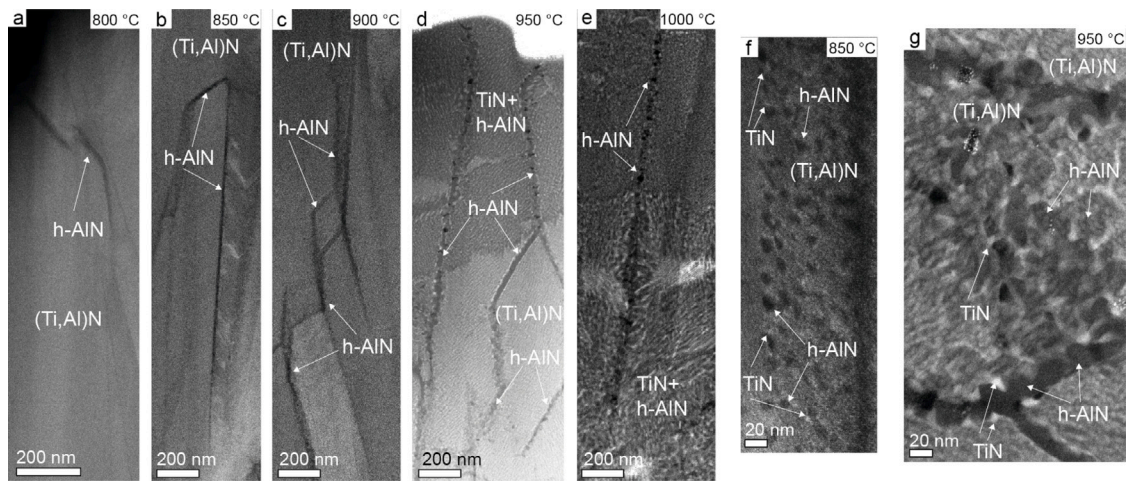


**Fig. 8.** HAADF STEM micrographs showing examples of h-AlN domains forming along grain boundaries after annealing at different temperatures. In (a)–(e) the grain boundaries are oriented along the viewing direction, in (f)–(g) at an angle to the viewing direction.

region of retained nano-lamellar structure in Fig. 6, which indicates that both grain boundaries and the grain interiors in the vicinity of the (Ti,Al)N/TiN interface are comparatively more stable than other parts of the coating. This will be further discussed in Section 3.4.

The h-AlN phase appears as a continuous layer along grain boundaries in many of the STEM micrographs. However, this is an effect stemming from the 2D projection of the 3D structure of the specimen. By investigating grain boundaries which are inclined with respect to the electron beam, e.g. in Fig. 8(f), it can be seen that the grain boundary is not covered by a continuous h-AlN layer, but decorated by discrete domains of h-AlN with a size of around 10–12 nm. Small brighter domains can also be seen next to the h-AlN domains, indicating the formation of TiN. Similarly, an example of a grain boundary in the coating annealed at 950 °C can be seen in Fig. 8(g). The h-AlN domains covering the grain boundary have a size of around 30–40 nm and have grown together, compared to the discrete h-AlN domains that decorate the grain boundaries in the coating annealed at 850 °C (Fig. 8(f)). Brighter TiN domains forming alongside the darker h-AlN domains are clearly visible also after annealing at 950 °C.

The TiN and h-AlN domains forming along the grain boundaries are not randomly distributed. As can be seen in Fig. 7, the TiN domains are distributed along the edges of grain boundary regions, towards the remaining (Ti,Al)N grains, forming bright lines. Meanwhile, the h-AlN domains are distributed along the centre of the grain boundary regions. Further investigation revealed that this distribution of TiN domains and h-AlN domains also to some extent is a projection effect. A (Ti,Al)N grain in the coating that was annealed at 950 °C was put at the [101] zone axis and the h-AlN and TiN domains found along the grain boundaries of the grain were investigated, see Fig. 9. In this view the domain distribution in the grain boundary region is not symmetric, but instead TiN is found only on one side of the h-AlN, see Fig. 9(b) and (f). FFTs extracted for h-AlN domains and (Ti,Al)N using high resolution BF STEM micrographs gives an orientation relationship between h-AlN (h) and (Ti,Al)N (c), where  $\{001\}_h \parallel \{111\}_c$  and  $\langle 100 \rangle_h \parallel \langle 101 \rangle_c$  (Fig. 9(c)–(e)). This corresponds to close-packed planes parallel to close-packed planes in both materials, and is a common relationship between hexagonal and cubic materials, including (Ti,Al)N and h-AlN [41]. The orientation relationship allowed identification of which of the two adjacent (Ti,Al)N grains was the parent to the domain (the grain on the right hand side), and it can be seen that the h-AlN domain formed closest to the parent, with TiN domains located outside (to the left of) it (Fig. 9(b)). Thus, the symmetric distribution of domains seen in Fig. 7(b)–(d), with a central region of h-AlN and flanking TiN, probably stems from an overlap between domains forming from the two neighbouring (Ti,Al)N grains.

We note that grain boundary phases were previously reported in a fully decomposed coating annealed for 5 min at 1300 °C [25], where it was inferred from STEM DF to be TiN. A possible explanation for this difference in observation could be the difference in temperature, with temperatures up to at least 1000 °C permitting the formation of mainly h-AlN, along grain boundaries. However, lack of micrographs taken of grain boundaries at higher magnification in [25], makes it hard to compare the results obtained in the different works.

### 3.3.3. Domain size

While projection effects prevent reliable size measurements of the h-AlN and TiN domains forming inside the (Ti,Al)N grains using STEM, a qualitative difference in size for the domains were found throughout the coating after annealing at 1000 °C, with larger domains in the lower part of the coating compared to the upper part. As the domains are stacked upon each other, they will give rise a modulation of the intensity in the HAADF STEM micrographs that differs through the thickness of the coating, see Figs. 10(a)–(d) for examples. The size of the domains giving rise to the modulation in intensity in Figs. 10(a) and (c) is estimated to be approximately 5 nm in the upper part of the coating and 15 nm in the lower part of the coating from the frequency distribution obtained when performing a FFT on the micrographs. The local observations from STEM can be compared to the more statistically averaged CSTnD data, where the average size of coherently diffracting domains,  $D$ , can be approximated by the Scherrer equation:

$$D \approx \frac{0.9\lambda}{W \cos \theta} \quad (3)$$

where  $W$  is the full width at half maximum (FWHM) of the diffraction peak at  $2\theta$ . Here it should be noted that Eq. (3) only provides a rough estimate of the domain size, and that the fact that instrumental broadening contribution to the FWHM was not considered, results in an underestimation of the size. We also note that the presence of residual stresses, which would lead variations in peak position along the Debye–Scherrer rings, could lead to artificially broadening of the peaks in the azimuthally integrated data. We therefore compared the domain size obtained from azimuthally integrated diffractograms (Fig. 3) with values obtained by “caking” the data into 10° sectors and fitting each sector separately. The difference between the two methods was very small (on average within  $\pm 5\%$ ), indicating the effect of residual stresses on the measured peak width (and hence domain size) was negligible. However, fitting of caked data lead to problems for samples annealed at 850 and 900 °C, as the h-AlN peak intensity in the individual cakes was very low, and we therefore chose to present the values obtained from fitting of azimuthally averaged data. The h-AlN domain size calculated from the 100 peak and the corresponding normalized intensity of the

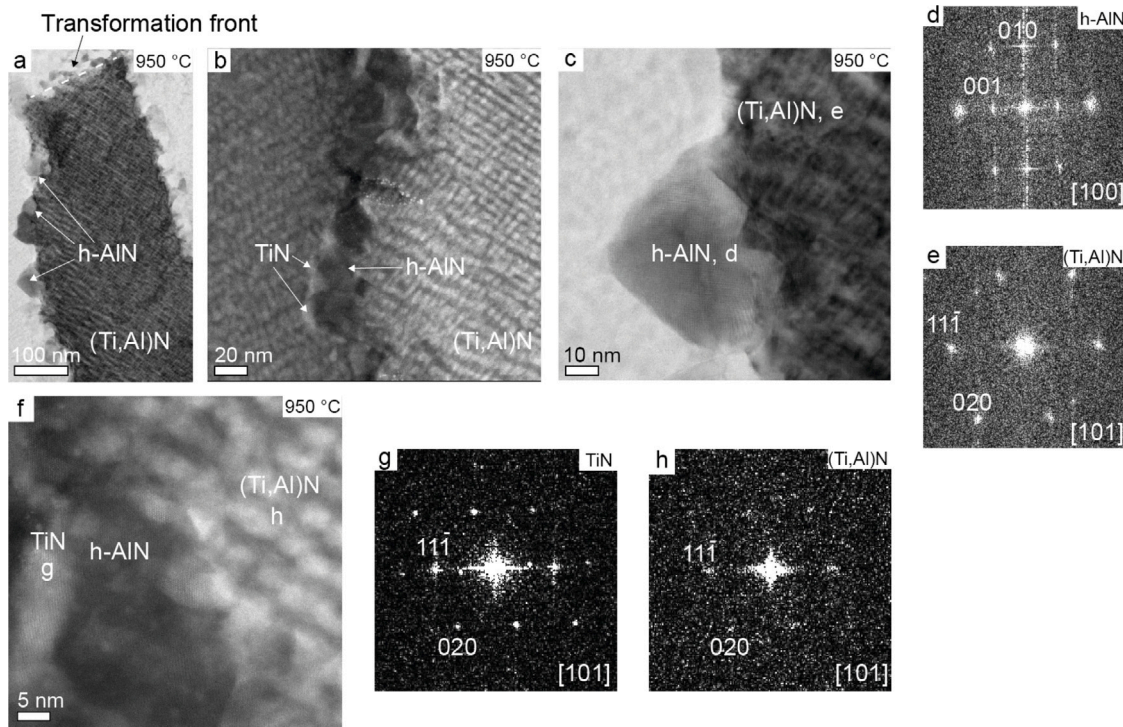


**Fig. 9.** STEM micrographs showing examples of h-AlN and TiN domains forming along a grain boundary after annealing at 950 °C. (a) and (c) are BF and (b) and (f) are HAADF STEM images. (d) and (e) are FFTs extracted from (c), giving the orientation relationship between h-AlN domains forming along grain boundaries and the surrounding (Ti,Al)N grains. (g) and (h) are FFTs extracted from (f), showing the formation of TiN along grain boundaries.

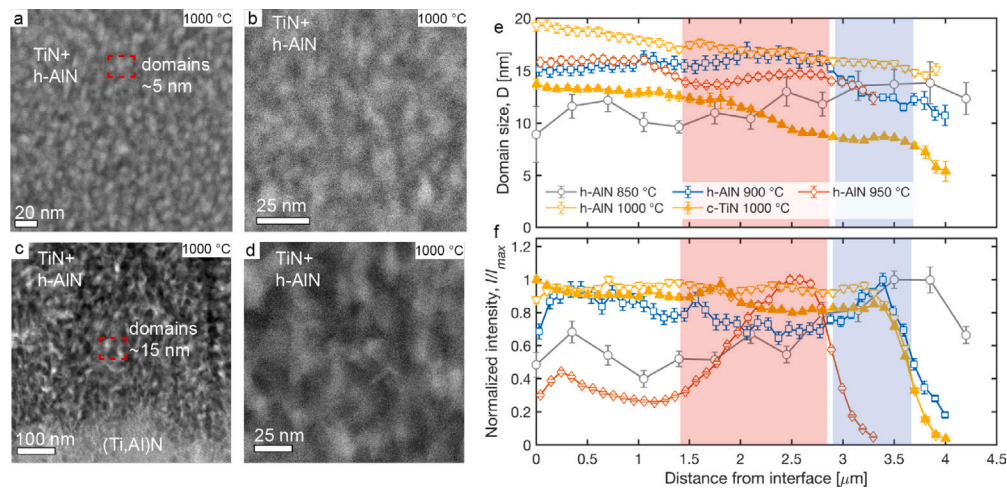


**Fig. 10.** (a)–(d) HAADF STEM micrographs showing examples of the decomposed nanostructure in the grain interior in the outer, (a) and (b), and inner, (c) and (d), part of the coating after annealing at 1000 °C. (e) Coherently diffracting domain size,  $D$ , determined by applying the Scherrer equation to the h-AlN 100 and TiN 200 peaks; and (f) Normalized integrated intensity (divided by the maximum integrated intensity observed at each temperature) of the same peaks as in (e), as functions of distance from the (Ti,Al)N/TiN interface for the samples annealed at 850, 900, 950 and 1000 °C. Blue and red areas indicate the regions where the intensity increases at 900 and 950 °C, respectively, which correspond to regions where bulk transformation is observed in the STEM images. (For interpretation of the references to colour in this figure legend, the reader is referred to the web version of this article.)

peak, is shown in Fig. 10 for samples annealed between 850 and 1000 °C.

The coating annealed at 850 °C shows a relatively constant domain size throughout the thickness, with a size of around 10–13 nm. This corresponds to the early stages of grain boundary h-AlN formation, and the size is consistent with the STEM image in Fig. 8(e). The intensity increases gradually towards the top of the coating, indicating a larger transformed volume.

After the 900 °C anneal, the domain size is approximately constant through the thickness, except close to the surface (blue shaded region),

and slightly larger than that after annealing at 850 °C. This is reasonable, as the size will correspond to the grain boundary h-AlN domains in the inner part (which had coarsened compared to at 850 °C), and to the average of grain boundary and intergranular domains in the outermost part. The intragranular domains are smaller, and consequently the average domain size drops close to the surface. This directly correlates with the increase in peak intensity in the near surface region, as the signal strength would be the sum of the grain boundary and intragranular domains. Note that the decrease in intensity observed in the outermost part is a result of the finite beam size traversing the upper surface in combination with slight misalignment of the coatings, which will smear



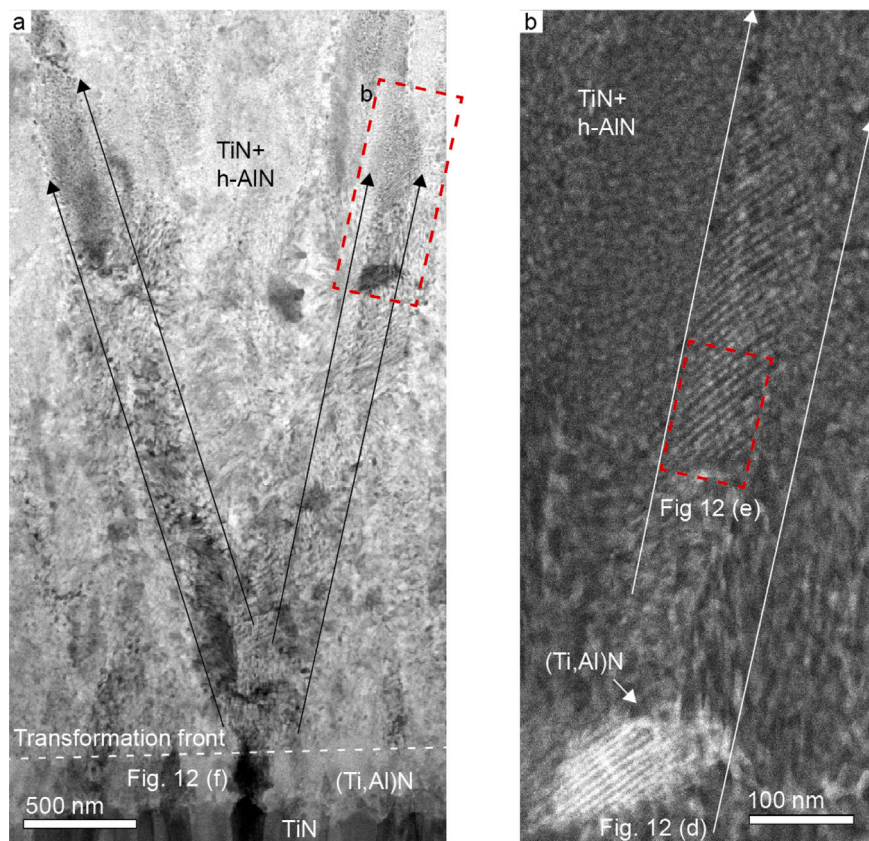


**Fig. 11.** STEM micrographs of the coating that has been annealed at 1000 °C, (a) is BF and (b) is HAADF. A TiN grain in the lower TiN layer has been oriented along the [101] zone-axis, orienting the remnants of the two (Ti,Al)N grains that nucleated on top of said TiN grain also along the [101] zone-axis.

the signal across the surface. This is also the likely reason for slight differences in the extent of the bulk transformation at 900 and 950 °C in Fig. 10 compared to STEM images from thin foils where no such smearing occurs.

After annealing at 950 °C the behaviour is similar, but the decrease in  $D$  and the associated increase in normalized intensity occurs closer to the interface, consistent with the decomposition having occurred to a much larger depth in the coating (Figs. 3(e) and 5(c)). The measured size in the outer part is expected to be dominated by the signal from the intragranular domains, as the volume fraction of grain boundary regions is considerably smaller. We also note that the domain size in the untransformed region has not increased noticeably, consistent with previous STEM observations.

In the coating annealed at 1000 °C there is a continuous decrease in the h-AlN domain size through the coating (from around 20 nm at the interface to around 15 nm at the surface), while the normalized intensity remains almost constant. In this case, the size is the average of intragranular and grain boundary domains throughout the coating. As the former was shown to coarsen in the inner parts (compare Fig. 10(a,b) and (c,d)), and the latter was approximately independent of position, this is again a reasonable behaviour. For the coating annealed at 1000 °C, the domain size for TiN could also be obtained from the TiN 200 peak, and can be seen to follow the behaviour of h-AlN at the same temperature, but having a smaller size (Fig. 10), consistent with STEM observations.

### 3.4. Spinodal decomposition of the nano-lamellar structure

As previously mentioned, the Ti(Al)N lamellae in coatings annealed at 900 °C and above are substantially broader compared to the lamellae found in the as-deposited coating. For the coatings annealed at 900 °C and 950 °C it is straightforward to image the nano-lamellae structure

after annealing. Large parts of the coatings remains untransformed and suitable grains can be tilted to a zone-axis for imaging. For the coating annealed at 1000 °C, only small parts of grains spread through the transformed coating remain as (Ti,Al)N. These remaining domains are usually only around some hundred nm in size, making them more challenging to investigate. However, we have previously shown that during CVD of (Ti,Al)N on TiN layers with well pronounced {211} texture, pairs of (Ti,Al)N grains will nucleate epitaxially on TiN grains and grow inclined along two different [111] directions [42]. By tilting a TiN grain in the underlying TiN layer to a zone-axis, the pair of (Ti,Al)N grains that have nucleated on it will also be brought to a zone axis. In such way domains of untransformed (Ti,Al)N in the coating that has been annealed at 1000 °C can be brought to a suitable zone-axis for imaging the nano-lamellae structure. It also makes it possible to compare the nanostructure of an untransformed domain with the rest of the grain that has transformed and the part of the grain along the lower (Ti,Al)N/TiN interface that is below the transformation front. Fig. 11 and Fig. 12(d)–(f) are examples of this.

After annealing at 900 °C the Ti(Al)N lamellae have a width of approximately 3 nm compared to 1.8 nm for the as-deposited coating, notwithstanding any minor variations in periodicity, see Figs. 12(a) and (b) for typical examples. One possible explanation would be that the two different types of lamellae begin to fuse together and average out the difference in Ti:Al ratio. However, this would go against the well documented drive for (Ti,Al)N to undergo spinodal decomposition when annealed, and the CSTnD data does not show the diffraction peaks for the Al(Ti)N lamellae shifting towards larger  $d$ -spacing. Instead, the situation can be better understood by remembering that a STEM micrograph is a 2D projection of the 3D structure of the lamellae. The Ti(Al)N lamellae in the annealed coatings are not only wider, but also show larger variations in thickness along the lamellae compared to the as-deposited coating. This can be explained by growth



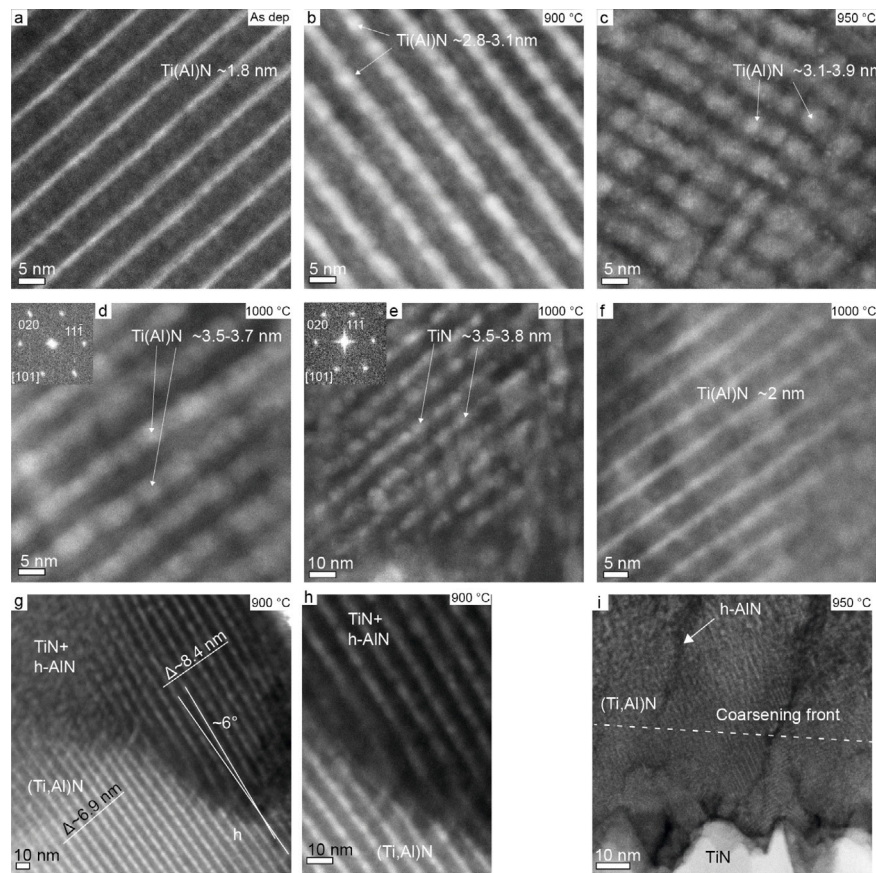


**Fig. 12.** HAADF STEM micrographs of the nano-lamella structure. (a) As-deposited coating; (b) and (c) untransformed regions in coatings annealed at 900 and 950 °C, respectively; (d) and (e) show the structure in the untransformed and transformed parts, respectively, of the same partially transformed grain in the middle of the coating annealed at 1000 °C; (f) Structure of a grain within the stable nano-lamellae region close to the (Ti,Al)N/TiN interface in the sample annealed at 1000 °C; (g) A partially transformed grain in the coating annealed at 900 °C, with a magnification of the boundary between the two parts of the grain shown in (h). (i) (Ti,Al)N/TiN interface in the coating annealed at 950 °C. All grains are oriented along a [101] zone axis.

of pre-existing Ti-rich domains within the Ti(Al)N layer, which in the 2D projections are stacked upon each other, explaining why the lamellae appear broader after annealing at 900 °C. This is seen also in untransformed parts of the coatings annealed at 950 and 1000 °C, see Figs. 12(c) and (d) for examples. The Ti(Al)N lamellae are broader in both these coatings compared to the coating annealed at 900 °C, around 3.1–3.9 nm in the former and 3.5–3.7 nm in the latter and even more heterogeneous in structure with what looks like overlapping discrete domains forming along the plane of the Ti rich lamella. Note that the coating annealed at 950 °C is thinner compared to the other coatings and the periodicity of the nano-lamellae structure is shorter, and as a consequence the broad Ti(Al)N lamellae are occasionally overlapping. However, the CSTnD data still indicates that this is best understood as two sets of domains moving away from each other in composition, not towards, with broadened diffraction peaks stretching towards pure cubic c-AlN and TiN. Most of the (Ti,Al)N has transformed to h-AlN and TiN in the coating that was annealed at 1000 °C, and the signal from the remaining (Ti,Al)N phase visible in the CSTnD plot is clearly shifted towards smaller  $d$ -spacing compared to the signal visible in the CSTnD plot for the as-deposited coating. This indicates that Ti has diffused from the Al(Ti)N lamellae, leaving them very close to (if not fully) pure c-AlN. FFTs extracted for Al(Ti)N lamellae in Fig. 12(d) gives a lattice parameter of around 4.06 Å, further supporting that the Al(Ti)N lamellae are either pure, or close to pure, c-AlN. In contrast, FFTs extracted from the Ti(Al)N lamellae gives a lattice parameter of around 4.17–4.25 Å, matching Ti(Al)N lamellae with very high Ti content.

Remnants of the nano-lamellae structure in regions that had decomposed in the coatings annealed at 900 and 1000 °C were investigated

and compared to the nano-lamellae structure in regions that had not. Fig. 12(e) is from a transformed region in the same grain that Fig. 12(d) is from and where remnants of the nano-lamellae structure is still visible. An FFT extracted from the transformed region (Fig. 12(e)) gives a lattice parameter of around 4.25 Å, matching pure TiN and indicating that the (Ti,Al)N grain has decomposed partly to TiN domains, which to a large extent has the same orientation as the original (Ti,Al)N grain. Interestingly, the pure TiN domains seen in Fig. 12(e) are not much different in size compared to the ones seen in Fig. 12(d). Figs. 12(g)–(h) show examples from a partially transformed grain in the top of the coating annealed at 900 °C. The width of the Ti(Al)N lamellae changes only slightly between the transformed and untransformed region. In contrast, the Al(Ti)N lamellae, where most of the h-AlN will form, broaden substantially in the transformed region (~5.2 nm) compared to the untransformed (~3.8 nm), resulting in a change of periodicity from ~6.9 to ~8.4 nm. Additionally, a rotation of the lamellae of around 6° along the transformation front can be seen, illustrating the volumetric expansion involved in the formation of h-AlN.

It has been suggested that the spatial inhomogeneity of the decomposition process (more pronounced decomposition in the outer part) originates from local variations in thermal stability, as the smaller grain size and lower defect density in the inner part would limit the nucleation [25]. Here we note that the decomposition starts at the surface, which suggests that the ability to relax the compressive transformation stresses controls where the process starts, rather than microstructural features. Nevertheless, as discussed in Section 3.3, a band of untransformed nano-lamellae (Ti,Al)N is present at the (Ti,Al)N/TiN interface after annealing at 1000 °C, see Fig. 6(a). Contrary to the above-mentioned regions of untransformed (Ti,Al)N found dispersed within

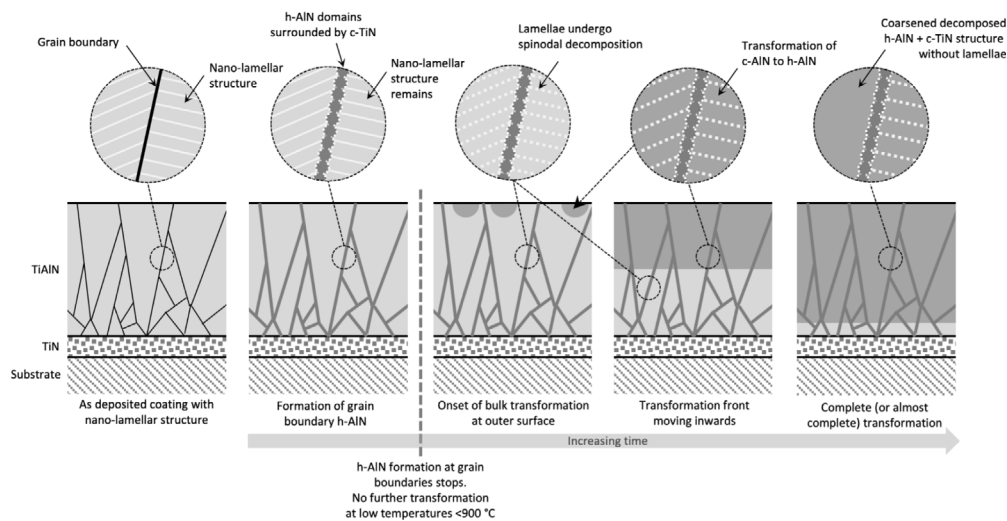


Fig. 13. Schematic showing the suggested decomposition process.

the parts of the coating which had undergone bulk transformation (Figs. 6(b) and 12(d)), the nano-lamellae structure in the band close to the interface had not undergone coarsening. Instead, the width and periodicity of the as-deposited coating is retained. The band is not constituted of entire small grains, but are rather the lower part of the larger columnar grains in the coatings. Furthermore, a much lower amount of grain boundary h-AlN was found in this region, as previously mentioned. A similar situation was found for the coating annealed at 950 °C. The microstructure in the lower part of the coating has begun to coarsen through growth of Ti and Al rich domains. However, along the (Ti,Al)N/TiN interface there is a band of (Ti,Al)N where the coarsening has not begun, and where there is a limited formation of h-AlN along the grain boundaries, see Fig. 12(i). These observations do indeed support the hypothesis that the thermal stability varies throughout the coating, with the innermost part being more resistant to decomposition (although this variation is not the reason for the inhomogeneous decomposition). The reason for the increased stability in the vicinity of the (Ti,Al)N/TiN interface is not clear at present, and will require further detailed studies. However, the fact that the untransformed band did not consist of individual small grains, but rather the bottom regions of large elongated grains, indicates that it is not the grain size which stabilizes the nano-lamellar structure.

As suggested by Tkadletz et al. [26], most of the changes in the nano-lamellar structure of (Ti,Al)N before h-AlN formation occur in the Ti(Al)N lamellae, with in-diffusion of Ti from Al(Ti)N lamellae. The change is probably driven by spinodal decomposition, but could also possibly be influenced by differences in surface energies between domains. The fact that most of the changes in nanostructure occur in the plane of the Ti(Al)N lamellae makes TEM image interpretation difficult. Thus, to get a better understanding for the change in nanostructure and the factors driving it, further studies using a technique capable of resolving the structure and chemical distribution of the decomposing lamellae in 3D, such as APT, is required.

#### 4. Summary and conclusions

In summary, we have investigated the thermal stability of nano-lamellar  $\text{Ti}_{0.2}\text{Al}_{0.8}\text{N}$  coatings deposited by CVD, which were exposed to isothermal annealing at different temperatures in the range of 800–1000 °C for 3 h in Ar, using a combination of high-resolution STEM and CSTnD. The results generally agree well with previous studies [25], but the experimental techniques and choice of annealing conditions allowed a more detailed picture to emerge, in particular with respect to the spatial dependence of the decomposition process and subtle changes occurring at lower temperatures. The following main observations have been made:

- At temperatures up to 850 °C, very limited formation of h-AlN occurred. The decomposition was localized to grain boundaries, where discrete domains of h-AlN, and smaller associated TiN domains, could be observed. Formation of grain boundary h-AlN occurred throughout the thickness of the coating.
- At 900 °C, more pronounced grain boundary h-AlN formation occurred, but the start of a bulk decomposition was also observed. The outermost part of the coating (some 200–300 nm) showed transformation of the grain interior through spinodal decomposition. In the untransformed region, Ti-rich domains had started to form within the Ti(Al)N nano-lamellae.
- The sample annealed at 950 °C showed a partially transformed structure, with grain boundary h-AlN throughout the coating thickness and bulk transformation through spinodal decomposition in the upper third. This resulted in an increase in the thickness of the Al(Ti)N lamellae and an increase in periodicity.
- After 3 h annealing at 1000 °C, the entire coating had transformed into TiN+h-AlN, except for a thin layer above the (Ti,Al)N/TiN interface, where the (Ti,Al)N appears to be stabilized.

We conclude that decomposition of (Ti,Al)N into h-AlN and TiN begins along grain boundaries. This is likely a result of the free volume associated with these boundaries, which allows the volume expansion due to formation of h-AlN to be more readily accommodated. However, the growth of grain boundary h-AlN ceases relatively quickly, due to the restrictions of the surrounding grains and developing (local) compressive stresses. At the lower annealing temperatures, this effectively stops further transformation from occurring, at least within the annealing times used in this study, as the driving force for bulk transformation of the grain interiors is too low.

At higher temperatures, the grain boundary h-AlN formation is followed by bulk transformation of the nano-lamellar grains by spinodal decomposition, starting at the outer surface and sweeping inwards through the coating. As the decomposition is initially very localized, being confined to the top 200–300 nm of the coating after 3 h annealing at 900 °C, the start of the decomposition process from the top is more likely a result of the capability of the near-surface region to accommodate volumetric expansion rather than a difference in defect content and homogeneity between the inner and outer parts. Initial decomposition of Ti(Al)N lamellae is followed by transformation of Al(Ti)N lamellae, finally leading to a coarsened structure with Ti-rich domains in a h-AlN matrix. The bulk transformation is relatively slow, only reaching approximately one third through the coating thickness

after 3 h at 950 °C, and is preceded by formation of grain boundary h-AlN throughout the entire thickness.

While the current study involves samples annealed for a constant time at different temperatures, we suggest that the decomposition process can be generalized to describe the structural evolution with time, as schematically shown in Fig. 13.

### Declaration of competing interest

The authors declare the following financial interests/personal relationships which may be considered as potential competing interests: Dirk Stiens and Thorsten Manns are employees of Walter AG, a commercial cutting tool manufacturer.

### Acknowledgements

Funding from “CVD 2.0”, a Swedish Foundation for Strategic Research program via SSF contract RMA15-0048 is gratefully acknowledged. We acknowledge the MAX IV Laboratory for time on the NanoMAX beamline under proposal 20170201. Research conducted at MAX IV, a Swedish national user facility, is supported by the Swedish Research council under contract 2018-07152, the Swedish Governmental Agency for Innovation Systems under contract 2018-04969, and Formas under contract 2019-02496. We acknowledge DESY (Hamburg, Germany), a member of the Helmholtz Association HGF, for the provision of experimental facilities. Parts of this research were carried out at the P03 beamline at PETRA III, where beamtime was allocated for proposal I-20180338 EC. The assistance of Ren Qiu and Siamak Shoja during the synchrotron experiments is gratefully acknowledged. The work was performed in part at the Chalmers Material Analysis Laboratory, CMAL.

### References

- [1] P.H. Mayrhofer, C. Mitterer, L. Hultman, H. Clemens, Microstructural design of hard coatings, *Prog. Mater. Sci.* 51 (8) (2006) 1032–1114, <http://dx.doi.org/10.1016/j.pmatsci.2006.02.002>.
- [2] P. Mayrhofer, R. Rachbauer, D. Holec, F. Rovere, J. Schneider, Protective transition metal nitride coatings, in: *Comprehensive Materials Processing*, Elsevier, 2014, pp. 355–388, <http://dx.doi.org/10.1016/B978-0-08-096532-1.00423-4>.
- [3] C. Mitterer, PVD and CVD Hard Coatings, vol. 2, Elsevier Ltd, 2014, <http://dx.doi.org/10.1016/B978-0-08-096527-7.00035-0>.
- [4] F. Vaz, L. Rebouta, M. Andritschky, M.F. Da Silva, J.C. Soares, Thermal oxidation of  $Ti_{1-x}Al_xN$  coatings in air, *J. Eur. Ceram. Soc.* 17 (15–16) (1997) 1971–1977, [http://dx.doi.org/10.1016/S0955-2219\(97\)00050-2](http://dx.doi.org/10.1016/S0955-2219(97)00050-2).
- [5] S. PalDey, S.C. Deevi, Single layer and multilayer wear resistant coatings of (Ti,Al)N: A review, *Mater. Sci. Eng. A* 342 (1–2) (2003) 58–79, [http://dx.doi.org/10.1016/S0921-5093\(02\)00259-9](http://dx.doi.org/10.1016/S0921-5093(02)00259-9).
- [6] A. Höling, L. Hultman, M. Odén, J. Sjölin, L. Karlsson, Mechanical properties and machining performance of  $Ti_{1-x}Al_xN$ -coated cutting tools, *Surf. Coat. Technol.* 191 (2–3) (2005) 384–392, <http://dx.doi.org/10.1016/j.surfcoat.2004.04.056>.
- [7] L. Chen, J. Paulitsch, Y. Du, P.H. Mayrhofer, Thermal stability and oxidation resistance of Ti–Al–N coatings, *Surf. Coat. Technol.* 206 (11–12) (2012) 2954–2960, <http://dx.doi.org/10.1016/j.surfcoat.2011.12.028>.
- [8] H. Holleck, Metastable coatings - Prediction of composition and structure, *Surf. Coat. Technol.* 36 (1–2) (1988) 151–159, [http://dx.doi.org/10.1016/0257-8972\(88\)90145-4](http://dx.doi.org/10.1016/0257-8972(88)90145-4).
- [9] K. Kutschej, P.H. Mayrhofer, M. Kathrein, P. Polcik, R. Tessadri, C. Mitterer, Structure, mechanical and tribological properties of sputtered  $Ti_{1-x}Al_xN$  coatings with  $0.5 \leq x \leq 0.75$ , *Surf. Coat. Technol.* 200 (7) (2005) 2358–2365, <http://dx.doi.org/10.1016/j.surfcoat.2004.12.008>.
- [10] C. Wüstefeld, D. Rafaja, V. Klemm, C. Michotte, M. Kathrein, Effect of the aluminium content and the bias voltage on the microstructure formation in  $Ti_{1-x}Al_xN$  protective coatings grown by cathodic arc evaporation, *Surf. Coat. Technol.* 205 (5) (2010) 1345–1349, <http://dx.doi.org/10.1016/j.surfcoat.2010.07.057>.
- [11] D. Holec, R. Rachbauer, L. Chen, L. Wang, D. Luef, P.H. Mayrhofer, Phase stability and alloy-related trends in Ti–Al–N, Zr–Al–N and Hf–Al–N systems from first principles, *Surf. Coat. Technol.* 206 (7) (2011) 1698–1704, <http://dx.doi.org/10.1016/j.surfcoat.2011.09.019>.
- [12] B. Grossmann, N. Schalk, C. Czettl, M. Pohler, C. Mitterer, Phase composition and thermal stability of arc evaporated  $Ti_{1-x}Al_xN$  hard coatings with  $0.4 \leq x \leq 0.67$ , *Surf. Coat. Technol.* 309 (2017) 687–693, <http://dx.doi.org/10.1016/j.surfcoat.2016.11.015>.
- [13] I. Endler, M. Höhn, M. Herrmann, R. Pitonak, S. Ruppi, M. Schneider, H. van den Berg, H. Westphal, Novel aluminum-rich  $Ti_{1-x}Al_xN$  coatings by LPCVD, *Surf. Coat. Technol.* 203 (2008) 530–533, <http://dx.doi.org/10.1016/j.surfcoat.2008.04.098>.
- [14] I. Endler, M. Höhn, M. Herrmann, H. Holzschuh, R. Pitonak, S. Ruppi, H. van den Berg, H. Westphal, L. Wilde, Aluminum-rich TiAlCN coatings by Low Pressure CVD, *Surf. Coat. Technol.* 205 (2010) 1307–1312, <http://dx.doi.org/10.1016/j.surfcoat.2010.09.002>.
- [15] J. Keckes, R. Daniel, C. Mitterer, I. Matko, B. Sartory, A. Koepf, R. Weissenbacher, R. Pitonak, Self-organized periodic soft-hard nanolamellae in polycrystalline TiAlN thin films, *Thin Solid Films* 545 (2013) 29–32, <http://dx.doi.org/10.1016/j.tsf.2013.08.001>.
- [16] J. Todt, R. Pitonak, A. Köpf, R. Weissenbacher, B. Sartory, M. Burghammer, R. Daniel, T. Schöberl, J. Keckes, Superior oxidation resistance, mechanical properties and residual stresses of an Al-rich nanolamellar  $Ti_{0.05}Al_{0.95}N$  coating prepared by CVD, *Surf. Coat. Technol.* 258 (2014) 1119–1127, <http://dx.doi.org/10.1016/j.surfcoat.2014.07.022>.
- [17] J. Todt, J. Zalesak, R. Daniel, R. Pitonak, A. Köpf, R. Weissenbacher, B. Sartory, C. Mitterer, J. Keckes, Al-rich cubic  $Al_{0.8}Ti_{0.2}N$  coating with self-organized nanolamellar microstructure: Thermal and mechanical properties, *Surf. Coat. Technol.* 291 (2016) 89–93, <http://dx.doi.org/10.1016/j.surfcoat.2016.02.027>.
- [18] A. Köpf, J. Keckes, J. Todt, R. Pitonak, R. Weissenbacher, Nanostructured coatings for tooling applications, *Int. J. Refract. Met. Hard Mater.* 62 (2017) 219–224, <http://dx.doi.org/10.1016/j.jrmhm.2016.06.017>.
- [19] J. Zalesak, D. Holec, I. Matko, M. Petrenec, B. Sartory, N. Koutná, R. Daniel, R. Pitonak, J. Keckes, Peculiarity of self-assembled cubic nanolamellae in the TiN/AlN system: Epitaxial self-stabilization by element deficiency/excess, *Acta Mater.* 131 (2017) 391–399, <http://dx.doi.org/10.1016/j.actamat.2017.04.009>.
- [20] C. Saringer, M. Tkadletz, A. Stark, N. Schell, C. Czettl, N. Schalk, In-situ investigation of the oxidation behavior of metastable CVD- $Ti_{1-x}Al_xN$  using a novel combination of synchrotron radiation XRD and DSC, *Surf. Coat. Technol.* 374 (2019) 617–624, <http://dx.doi.org/10.1016/j.surfcoat.2019.05.072>.
- [21] R. Qiu, A. Forslund, O. Bäcké, A. Iyer, M. Sattari, W. Janssen, T. Manns, J. Kümmler, A. Ruban, D. Stiens, H.-O. Andén, M. Halvarsson, Effects of gas flow on detailed microstructure inhomogeneities in LPCVD TiAlN nanolamella coatings, *Materialia* 9 (2020) 100546, <http://dx.doi.org/10.1016/j.mta.2019.100546>.
- [22] A. Paseuth, K. Yamagata, A. Miura, M. Higuchi, K. Tadanaga, Deposition and analysis of Al-rich  $c-Al_xTi_{1-x}N$  coating with preferred orientation, *J. Am. Ceram. Soc.* 100 (2016) 343–353, <http://dx.doi.org/10.1111/jace.14549>.
- [23] A. Paseuth, Y. Kido, S. Imamura, K. Yamagata, A. Miura, K. Tadanaga, Thermal stability and cutting performance of Al-rich cubic  $Al_xTi_{1-x}N$  coating prepared by low-pressure chemical vapour deposition, *J. Ceram. Soc. Japan* 125 (2017) 913–918, <http://dx.doi.org/10.2109/jcersj.2.17152>.
- [24] R. Qiu, H. Aboulfadl, O. Bäcké, D. Stiens, H.O. Andén, M. Halvarsson, Atom probe tomography investigation of 3D nanoscale compositional variations in CVD TiAlN nanolamella coatings, *Surf. Coat. Technol.* 426 (September) (2021) <http://dx.doi.org/10.1016/j.surfcoat.2021.127741>.
- [25] M. Tkadletz, C. Hofer, C. Wüstefeld, N. Schalk, M. Motylenko, D. Rafaja, H. Holzschuh, W. Bürgin, B. Sartory, C. Mitterer, C. Czettl, Thermal stability of nanolamellar  $fcc-Ti_{1-x}Al_xN$  grown by chemical vapor deposition, *Acta Mater.* 174 (2019) 195–205, <http://dx.doi.org/10.1016/j.actamat.2019.05.044>.
- [26] M. Tkadletz, A. Lechner, N. Schalk, B. Sartory, A. Stark, N. Schell, C. Saringer, C. Mitterer, C. Czettl, Influence of spinodal decomposition and fcc-to-w phase transformation on global and local mechanical properties of nanolamellar  $cvd fcc-Ti_{1-x}Al_xN$  coatings, *Materialia* 11 (2020) 100696, <http://dx.doi.org/10.1016/j.mta.2020.100696>.
- [27] M. Meindlumer, S. Klima, N. Jäger, A. Stark, H. Hrubby, C. Mitterer, J. Keckes, R. Daniel, Stress-controlled decomposition routes in cubic AlCrN films assessed by in-situ high-temperature high-energy grazing incidence transmission X-ray diffraction, *Sci. Rep.* 9 (2019) 18027, <http://dx.doi.org/10.1038/s41598-019-54307-7>.
- [28] N. Jäger, M. Meindlumer, S. Spor, H. Hrubby, J. Julin, A. Stark, F. Nahif, J. Keckes, C. Mitterer, R. Daniel, Microstructural evolution and thermal stability of AlCr(Si)N hard coatings revealed by in-situ high-temperature high-energy grazing incidence transmission X-ray diffraction, *Acta Mater.* 186 (2020) 545–554, <http://dx.doi.org/10.1016/j.actamat.2020.01.026>.
- [29] J. Keckes, M. Bartosik, R. Daniel, C. Mitterer, G. Maier, W. Ecker, J. Vila-Comamala, C. David, S. Schoeder, M. Burghammer, X-ray nanodiffraction reveals strain and microstructure evolution in nanocrystalline thin films, *Scr. Mater.* 67 (2012) 748–751, <http://dx.doi.org/10.1016/j.scriptamat.2012.07.034>.
- [30] J. Zalesak, M. Bartosik, R. Daniel, C. Mitterer, C. Krywka, D. Kiener, P. Mayrhofer, J. Keckes, Cross-sectional structure–property relationship in a graded nanocrystalline  $Ti_{1-x}Al_xN$  thin film, *Acta Mater.* 102 (2016) 212–219, <http://dx.doi.org/10.1016/j.actamat.2015.09.007>.
- [31] A. Riedl, R. Daniel, J. Todt, M. Stefanelli, D. Holec, B. Sartory, C. Krywka, M. Müller, C. Mitterer, J. Keckes, A combinatorial X-ray sub-micron diffraction study of microstructure, residual stress and phase stability in TiAlN coatings, *Surf. Coat. Technol.* 257 (2014) 108–113, <http://dx.doi.org/10.1016/j.surfcoat.2014.03.045>.



- [32] C. Krywka, H. Neubauer, M. Priebe, T. Salditt, J. Keckes, A. Buffet, S.V. Roth, R. Doebrmann, M. Mueller, A two-dimensional waveguide beam for X-ray nanodiffraction, *J. Appl. Crystallogr.* 45 (2012) 85–92, <http://dx.doi.org/10.1107/S0021889811049132>.
- [33] A. Buffet, A. Rothkirch, R. Döhrmann, V. Körstgens, M.M. Abul Kashem, J. Perlich, G. Herzog, M. Schwartzkopf, R. Gehrke, P. Müller-Buschbaum, S.V. Roth, P03, the microfocus and nanofocus X-ray scattering (MiNaXS) beamline of the PETRA III storage ring: The microfocus endstation, *J. Synchrotron Radiat.* 19 (2012) 647–653, <http://dx.doi.org/10.1107/S0909049512016895>.
- [34] U. Johansson, D. Carbone, S. Kalbfleisch, A. Björling, M. Kahnt, S. Sala, T. Stankevic, M. Liebi, A. Rodriguez Fernandez, B. Bring, D. Paterson, K. Thånell, P. Bell, D. Erb, C. Weninger, Z. Matej, L. Roslund, K. Åhnberg, B. Norsk Jensen, H. Tarawneh, A. Mikkelsen, U. Vogt, NanoMAX: the hard X-ray nanoprobe beamline at the MAX IV Laboratory, *J. Synchrotron Radiat.* 28 (2021) 1935–1947, <http://dx.doi.org/10.1107/s1600577521008213>.
- [35] D. Carbone, S. Kalbfleisch, U. Johansson, A. Björling, M. Kahnt, S. Sala, T. Stankevic, A. Rodriguez-Fernandez, B. Bring, Z. Matej, P. Bell, D. Erb, V. Hardion, C. Weninger, H. Al-Sallami, J. Lidon-Simon, S. Carlson, A. Jerrebo, B. Norsk Jensen, A. Bjerme, K. Åhnberg, L. Roslund, Design and performance of a dedicated coherent X-ray scanning diffraction instrument at beamline NanoMAX of MAX IV, *J. Synchrotron Radiat.* 29 (3) (2022) 1–12, <http://dx.doi.org/10.1107/S1600577522001333>.
- [36] A. Björling, S. Kalbfleisch, M. Kahnt, S. Sala, K. Parfeniukas, U. Vogt, D. Carbone, U. Johansson, Ptychographic characterization of a coherent nanofocused X-ray beam, *Opt. Express* 28 (2020) 5069, <http://dx.doi.org/10.1364/oe.386068>.
- [37] G. Ashiotis, A. Deschildre, Z. Nawaz, J.P. Wright, D. Karkoulis, F.E. Picca, J. Kieffer, The fast azimuthal integration Python library: PyFAI, *J. Appl. Crystallogr.* 48 (2015) 510–519, <http://dx.doi.org/10.1107/S1600576715004306>.
- [38] G. Esteves, K. Ramos, C. Fancher, J. Jones, LIPRAS: Line-Profile Analysis Software, 2017, <http://dx.doi.org/10.13140/RG.2.2.29970.25282/3>.
- [39] B.H. Toby, R.B. Von Dreele, GSAS-II: the genesis of a modern open-source all purpose crystallography software package, *J. Appl. Crystallogr.* 46 (2013) 544–549.
- [40] L. Rogström, J. Ullbrand, J. Almer, L. Hultman, B. Jansson, M. Odén, Strain evolution during spinodal decomposition of TiAlN thin films, *Thin Solid Films* 520 (2012) 5542–5549, <http://dx.doi.org/10.1016/j.tsf.2012.04.059>.
- [41] D. Rafaja, C. Wustefeld, M. Dopita, M. Motylenko, C. Baehtz, C. Michotte, M. Kathrein, Crystallography of phase transitions in metastable titanium aluminium nitride nanocomposites, *Surf. Coat. Technol.* 257 (2014) 26–37, <http://dx.doi.org/10.1016/J.SURFCOAT.2014.01.039>.
- [42] M.B. Hassine, H.O. Andren, A.H. Iyer, A. Lotsari, O. Bäcke, D. Stiens, W. Janssen, T. Manns, J. Kummel, M. Halvarsson, Growth model for high-Al containing cvd TiAlN coatings on cemented carbides using intermediate layers of TiN, *Surf. Coat. Technol.* 421 (2021) 127361, <http://dx.doi.org/10.1016/J.SURFCOAT.2021.127361>.